

Tuning Threshold Voltage in Organic Electrochemical Transistors by Varying Doping of the Conjugated Polymer p(g3T2-T)

Marielena Velasco Enriquez

Thesis submitted for the degree of
Erasmus Mundus Master of Science
in Nanoscience and Nanotechnology,
graduation option Nanoelectronics

Supervisors:
Prof. Dr. Karl Leo
Prof. Dr. Steven De Feyter

Assessor:
PD Dr.rer.nat.habil. Hans Kleemann

Assistant-supervisor:
MSc. Anton Weissbach

© Copyright KU Leuven

Without written permission of the supervisors and the author it is forbidden to reproduce or adapt in any form or by any means any part of this publication. Requests for obtaining the right to reproduce or utilize parts of this publication should be addressed to Faculteit Ingenieurswetenschappen, Kasteelpark Arenberg 1 bus 2200, B-3001 Leuven, +32-16-321350.

A written permission of the supervisors is also required to use the methods, products, schematics and programmes described in this work for industrial or commercial use, and for submitting this publication in scientific contests.

Preface

Marielena Velasco Enríquez

Contents

Preface	i
Abstract	iv
List of Figures and Tables	v
1 Introduction	1
2 Background	3
2.1 Organic Semiconductors	3
2.1.1 Electronic Structure and Transport	3
2.1.2 Molecular Doping	4
2.2 Organic Mixed Ionic/Electronic Conductors (OMIECs)	6
2.2.1 Processes in OMIECs	7
2.3 Organic Electrochemical Transistors (OECTs)	9
2.3.1 Device Physics	9
2.3.2 Operation Modes	11
2.3.3 Important Figures of Merit	13
2.3.4 Side Reactions	16
3 Experimental Methods	19
3.1 Materials	19
3.2 Equipment	20
3.3 Software	21
3.4 Experimental Procedures	22
3.4.1 Preparation of films	22
3.4.2 Doping characterization of films	23
3.4.3 Fabrication of Organic Electrochemical Transistors	23
4 Results and Discussion	29
4.1 Doping characterization	29
4.1.1 Absorbance and dopants diffusion	29
4.1.2 Workfunction	30
4.1.3 Thickness, sheet resistance and resistivity	31
4.2 Fabrication of Organic Electrochemical Transistors	32
4.2.1 Influence of doping OECT channel	32
4.2.2 Stability on air of p(g3T2-T)	33
4.2.3 Reverse oxidation of undoped-p(g3T2-T)	33

CONTENTS

4.2.4	Solid-OECTs using undoped p(g3T2-T)	33
4.2.5	Solid-OECTs using doped-p(g3T2-T)	33
5	Conclusions and Outlook	37
A	Absorption of p(g3T2-T) doped with F6TCNNQ	41
B	PEDOT:PSS vs doped p(g3T2-T) as channel	43
	Bibliography	45

Abstract

Organic Electrochemical transistors (OECTs) exhibit advantageous properties, such as high transconductance and steep-slope switching, while operating at very low voltages. Although, their switching speed is comparatively slower than solid-state devices, it remains sufficient for applications in bioelectronics [1]. The gold standard semiconductor for p-type OECTs is PEDOT:PSS. However, its main drawback lies in its depletion-mode operation, which requires power to turn off the device. To minimize power consumption and improve stability, efforts have been made to the design conjugated polymers that allow accumulation-mode devices. One such polymer, 3-(2-(2-methoxyethoxy)ethoxy)thiophene (p(g3T2-T)) has demonstrated negative threshold voltages close to zero and high transconductance [2]. Furthermore, by doping p(g3T2-T) at various levels and drop-casting it as a gate, it has been possible to fine-tune the threshold voltage [3]. This study aims to adapt a microstructuring method for fabricating side-gated OECT devices that comprises different doping levels of F₄TCNQ and F₆TCNNQ in p(g3T2-T) and a solid-state electrolyte [4], the latter is deposited by inkjet printing. Additionally, the study aims to adjust the threshold voltage by utilizing these varying doping levels, while analyzing the stability and performance of the doped devices.

List of Figures and Tables

List of Figures

2.1	Energy level diagram of organic semiconductors	3
2.2	Degenerate and non-degenerate conjugated polymers	4
2.3	Scheme of doping processes in organic semiconductors	5
2.4	Representation of bipolaron formation introduced via doping	5
2.5	Formation of polaron, bipolaron, and bipolaron band	6
2.6	Material classes of OMIECs	7
2.7	Electronic transport mechanisms in OMIECs	8
2.8	Ionic transport mechanisms in OMIECs	9
2.9	Device physics of MOSFET vs OECT	10
2.10	Typical OECT structure and circuit model	10
2.11	Depletion- and accumulation-mode OECTs	11
2.12	Chemical structure of polymer g2T-T	12
2.13	Chemical structure and transconductance of g2T-T with side-chain engineering	13
2.14	OECTs benchmark with different OMIECs	14
2.15	Tuning of threshold voltage with different levels of doping p(g3T2-T) . .	15
2.16	Energy levels of neutral state of OMIECs related to oxygen reduction reactions potentials	17
3.1	Dynamic spin coating process to obtain undoped and doped films of p(g3T2-T))	22
3.2	Visualization of the workflow for Au-contacts patterning.	24
3.3	Visualization of the workflow for patterning undoped p(g3T2-T)	24
3.4	Visualization of the workflow for patterning doped p(g3T2-T)	25
3.5	Experimental setup to measure threshold voltage shift under ambient conditions.	26
3.6	Solid-OECT fabrication with undoped p(g3T2-T)	27
3.7	Solid-OECT fabrication with doped p(g3T2-T)	28
4.1	Color shift upon doping level increase	29
4.2	Absorbance spectra of different doping levels of p(g3T2-T)	30
4.3	Representation of the Fermi level shift upon doping	31

LIST OF FIGURES AND TABLES

4.4	Sheet resistance and resistivity drop upon doping	32
4.5	Micrographs of a patterned channel and gate p(g3T2-T) at different doping levels	33
4.6	Transfer characteristics and transconductance at different V_{DS} . a), c) and e) correspond to the exponential behavior of undoped, 5 mg/mL and 10 mg/mL doped, respectively.	34
4.7	Energy diagram of p(g3T2-T) and dopants F ₆ T CNNQ and F ₄ T CNNQ .	35

List of Tables

3.1	Cyclic Voltammetry parameters.	21
3.2	Electrochemical Impedance Spectroscopy parameters.	22
3.3	Composition of the solid-state electrolyte [4].	25
3.4	Composition of adhesion promoter.	27
4.1	Workfunction calculation from UPS measurements.	31
4.2	Sheet resistance and resistivity calculations for undoped and doped films of p(g3T2-T)	32
4.3	Maximum transconductance and μC^* product calculation	32

Chapter 1

Introduction

The field of organic electronics has witnessed significant advancements in recent years due to its potential biocompatibility, mechanical compliant, and other application-specific characteristics. Among the numerous types of organic devices, Organic Electrochemical Transistors (OECTs) have attracted considerable attention due to their unique capabilities such as high transconductance and steep-slope switching at low operation voltages, which give them potential for use in energy storage, bioelectronics, and neuromorphic devices.

Accumulation-mode transistors, devices that are normally in the OFF state at zero-gate-biased condition, rely on the use of undoped conjugated polymers. In contrast, the ability to precisely control and tune threshold voltage of an OECT can be achieved by manipulating the doping level of the mentioned conjugated polymer as shown by Tan et al. [3]. However, they fabricated devices that did not follow a complete microstructuring technique, limiting their integration into circuits.

The primary objective of this research is to address this missing information by developing a microstructuring method to fabricate accumulation-mode OECTs with controlled doping levels and enable their seamless integration into circuits. However, during the pursuit of this objective, it was identified that stability of the polymer and dopants in an electrochemical environment may pose challenges that need to be addressed as well. Therefore, this research project specifically aims to:

1. Characterize 3-(2-(2-(2-methoxyethoxy)ethoxy)ethoxy)thiophene (p(g3T2-T)) with varying doping levels of F₄TCNQ and F₆TCNNQ. This involves chemically modifying the conjugated polymer with different concentrations of dopant and analyzing their electronic structure, morphology and electrical properties using techniques such as UV-Vis spectroscopy, Ultraviolet Photoelectron Spectroscopy (UPS), Van Der Pauw method, Electrical Impedance Spectroscopy (EIS) and Cyclic Voltammetry (CV),
2. fabricate OECT devices, which involves utilizing the conjugated polymer at different doping levels, and adapting an existing method that combines electrode patterning techniques, spin-coating, photolithography and inkjet printing. The devices will be carefully optimized to ensure reproducibility and stability,

1. INTRODUCTION

3. assess doped polymer stability in OEET, which involves performing conductivity measurements over time and selecting an electrolyte composition that allows an stable performance, and
4. investigate the shift in threshold voltage through electrical characterization of the fabricated OEET devices with varying doping levels of F₄TCNQ and F₆TCNNQ.

The thesis is structured as follows: Chapter 1 provides an overview of organic electronics and the importance of the OEET threshold voltage, and outlines the motivation, goals, and structure of the thesis. Chapter 2 presents a comprehensive review of the relevant background information on Organic Semiconductors (OSCs), Organic Mixed Ionic Electronic Conductors (OMIECs), and Organic Electrochemical Transistors, and relevant research on tuning the threshold voltage of OEETs. Chapter 3 illustrates the Experimental Methods used in this research, describes the materials, equipment, software, and procedures to chemically dope the films and characterization method employed in the study. Finally, it outlines the fabrication and characterization process of OEET devices. In Chapter 4, the experimental results obtained are presented, from the characterization of the conjugated polymer at different doping levels and fabricated OEET devices. Analysis of the relationship between the doping level and the shift in threshold voltage. Finally, it discusses the implications of the findings and their relevance to the field. Lastly, Chapter 5 provides a summary of the research objectives and the extent to which they were achieved, suggests future research direction, and potential applications.

This study aims to adapt an existing protocol for the conjugated material p(g3T2-T), understand doping-dependent tuning of OEET threshold voltage, and establish a foundation for high-performance organic electronic devices by addressing research goals and following the proposed thesis structure.

Chapter 2

Background

2.1 Organic Semiconductors

Unlike inorganic semiconductors, organic semiconductors are lightweight, easy to chemically tune, mechanical flexible, and offer low-cost and low-temperature processing. All of these characteristics are responsible for the increased attention to this type of materials in the field of organic electronics.

2.1.1 Electronic Structure and Transport

Organic semiconductors are π -conjugated molecules that comprise mostly carbon and hydrogen atoms, with alternating multiple (sp^2 hybridization) and single (sp hybridization) bonds. The wavefunction of the sp^2 orbitals overlap so that electrons can be delocalized. Based on the size of the conjugated system, organic semiconductors can be divided into conjugated polymers and small molecules. The latter has the advantage of being ordered and its synthesis allows to obtain high purity material [5].

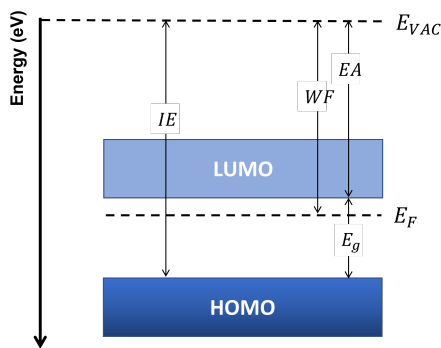


FIGURE 2.1: Energy level diagram of an n-type doped organic semiconductor.

The energy structure of organic semiconductors comprises a highest occupied molecular orbital (HOMO) and a lowest unoccupied molecular orbital (LUMO), that are analogous to the valence and conduction states, respectively, from inorganic

2. BACKGROUND

semiconductors. The difference between both energy levels corresponds to the energy gap (E_g) of the material, as represented in Figure 2.1. We could also defined i) the Fermi level (E_F) using the material work function (WF), ii) the ionization energy (IE, also referred as ionization potential, IP), using the HOMO energy, and iii) the electron affinity (EA), using the LUMO energy.

An organic semiconductor material could also be classified depending on whether the ground state is degenerate or non-degenerate. The former describes monomers that are energetically equivalent in the ground state, and in the latter, the opposite happens, commonly seen due to the energy difference of aromatic (benzoid) and quinoid structures [6], as exhibited in Figure 2.2.

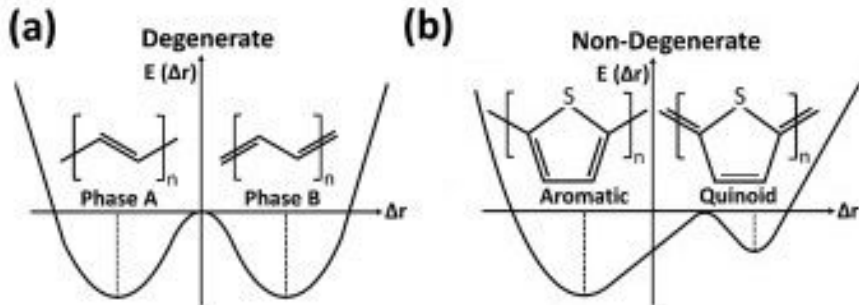


FIGURE 2.2: Potential energy change (electronic plus lattice distortion energy) in a) degenerate and b) non-degenerate ground-state-conjugated polymers. Extracted from reference [7].

Transport in an organic semiconductor creates changes in the bond-length alternation pattern. Since charge transport come together with a chain distortion, new quasiparticles are defined: solitons in degenerate molecules and polarons in non-degenerate molecules [8].

2.1.2 Molecular Doping

The basic principles of molecular doping are similar than in inorganic materials. A donor or acceptor entity is added to generate electrons or holes, as shown in Figure 2.3. While n-type dopants donate electrons to the lowest unoccupied molecular orbital (LUMO) states, the p-type dopants extract electrons from the highest occupied molecular orbital (HOMO) states, hence they create holes [9]. In other words, the Fermi level E_F of the polymer will shift towards the LUMO (or HOMO) level when there is n-type (or p-type) doping. This shift can be measured by spectroscopy techniques such as Ultraviolet Photoelectron Spectroscopy (UPS) at room temperature (RT) [10], although a bit limited by the penetration depth of the incoming electrons.

When doping occurs, the formation of a new quasiparticle named bipolaron occurs. For instance, if p-type dopant is introduced to a degenerate molecule (Figure 2.4), electrons are removed from double bonds, if we focus on just one event, while one carbon is left positively charged, the adjacent has an unpaired electron. This unpaired electron shifts down the polymer chain until reaching another unpaired

2.1. Organic Semiconductors

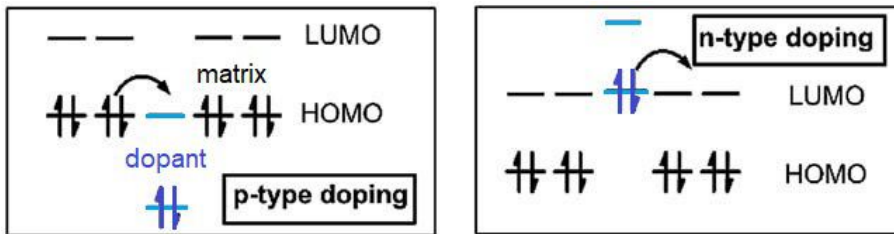


FIGURE 2.3: Schemes for p-type (left) and n-type (right) doping processes. Extracted from reference [9].

electron from a separated doping event, together they form a double bond, leaving aside two charged polarons: a bipolaron, which unlike a single polaron, it is stable [11].

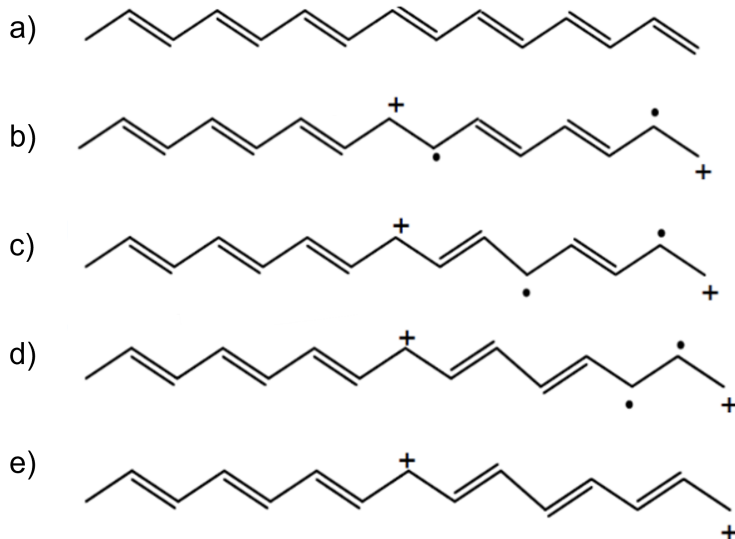


FIGURE 2.4: a) Structure of degenerate molecule. b) Electron extraction via doping. c) Unpaired electron shifting down. d) Unpaired electrons meet. e) Formation of double bond and two charged polarons: bipolaron.

The energy levels generated upon the formation of polarons and bipolarons are represented in Figure 2.5. As the doping density increases, the amount of bipolaron states increases as well, the overlapping of them led to the formation of bipolaron bands, and the energy difference between the two in-gap states i and i^* decreases (4th image in Figure 2.5). In addition to the new electronic states, the doped polymer will also exhibit distinct optical transitions that could be disclosed by UV-Vis-NIR spectroscopy, although not clearly defined quantitatively [7].

The use of small molecules is commonly reported as dopants for organic materials. Some strong acceptor (or electron-deficient) molecules that are widely used are 2,3,5,6-tetrafluoro-7,7,8,8-tetracyanoquinodimethane (F_4TCNQ) or 1,3,4,5,7,8-hexafluoro-

2. BACKGROUND

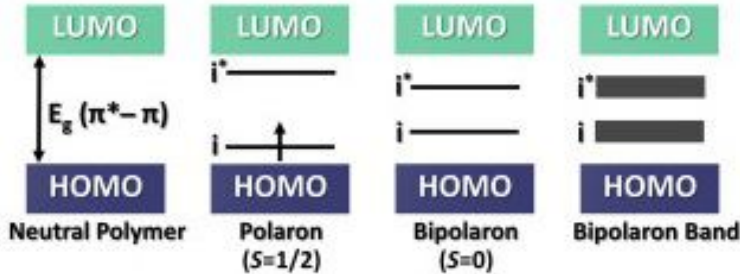


FIGURE 2.5: Potential energy change of aromatic and quinoid in the non-degenerate ground-state neutral conjugated polymer, and formation of polaron, bipolaron, and bipolaron bands upon doping. Extracted from reference [7].

7,7,8,8-tetracyanonorphthoquinodimethane (F_6TCNNQ), which also take part in this work. The latter exhibits a higher electronic affinity (-5.3 eV) or deep HOMO than F_4TCNQ (-5.2eV) meaning that it can abstract electrons more efficiently, specially from polymers with low ionization potential (less than 5eV) or shallow HOMO [12].

Among the different methods of molecular doping of conjugated polymers, Jacobs et al. compared a solution-mixed and solution sequential doping of P3HT (a thiophene-based polymer) doped with F_4TCNQ , both straightforward and easy methods for doping. Their work demonstrated that solution-mixed films are considerably rougher than solution-sequential films, affecting negatively its conductivity [13]. The fact that solution-sequential doped films possess better homogeneity, make it also more compatible with microstructuring processes such as photolithography. However, this comes at the expense of having less control over the doping levels compared to solution-mixed films [14].

2.2 Organic Mixed Ionic/Electronic Conductors (OMIECs)

Organic Mixed Ionic/Electronic conductors are organic semiconductors that allow the conduction of electrons (or holes) and ions, the latter set them apart from other organic semiconductors. Commonly structured with polar side chains, they have been identified as a promising class of materials for the field of bioelectronics [15]. Initially investigated for batteries and super-capacitors [16] [17], where the induction of charges in a semiconducting polymer was the main objective. OMIECs have rapidly grown to include other applications, among them, our focus: OECTs.

Paulsen et al. classified OMIECs into six different categories according to whether they *intrinsically contain ionic charge*” (I, III, V) or not (II, IV, VI), the latter “*contain polar moieties that can solvate ions*”. Another distinction among the categories is whether the conjugated system comprises a single material (homogeneous, type V and VI) or two-component, more complex systems or block co-polymers materials (heterogeneous, type I, II, III, IV)[18], an schematic representation is shown in Figure 2.6.

2.2. Organic Mixed Ionic/Electronic Conductors (OMIECs)

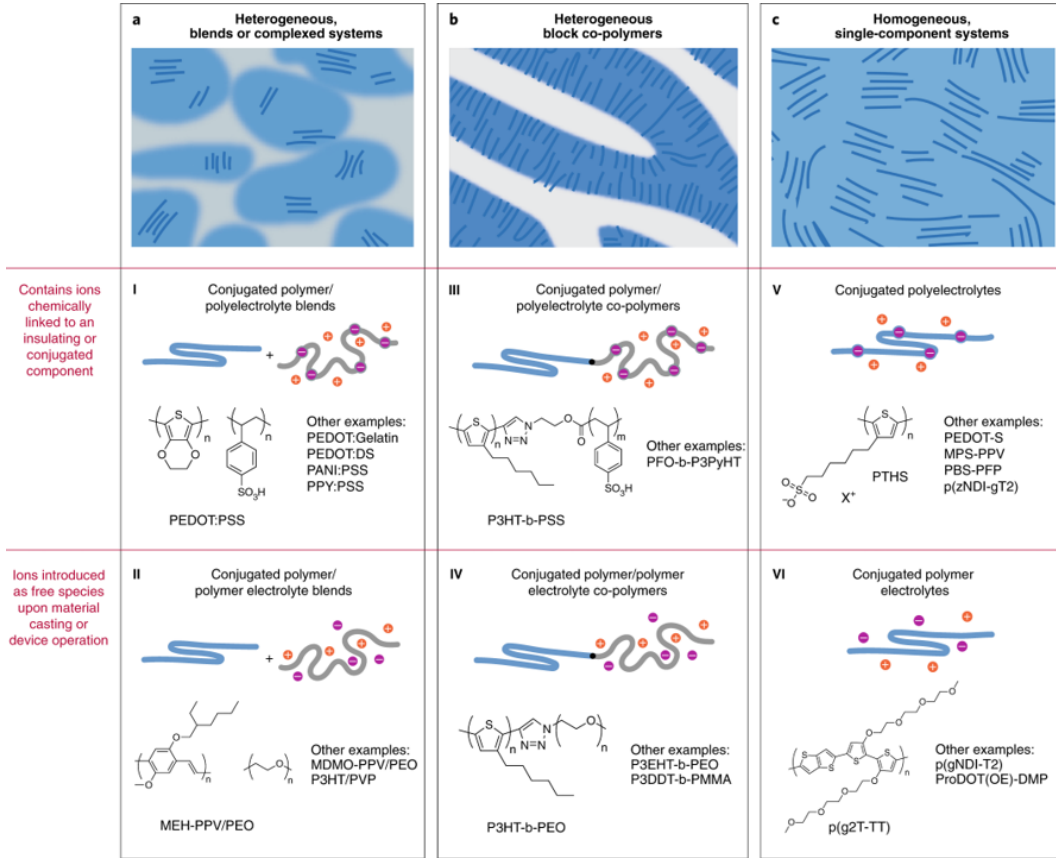


FIGURE 2.6: **OMIECs classes.** a) Heterogeneous blends of an conducting conjugated polymer with (I) a polyelectrolyte or (II) an ion-solvating polymer electrolyte. b) Heterogeneous block copolymers of a conducting conjugated polymer with (III) a polyelectrolyte or (IV) an ion-solvating polymer electrolyte. c) Fully conjugated (V) polyelectrolytes and (VI) ion-solvating polymer electrolytes. Extracted from reference [18].

2.2.1 Processes in OMIECs

2.2.1.1 Ionic-electronic interactions

The presence of electronic charge in OMIECs requires also the presence of excess ionic charge, so charge in the system remain balance. In the case of types II, IV and VI OMIECs, the so-called stabilizing electrochemical doping is achieved by the presence of mobile ions, that act as free charges, the remaining type of OMIECs, on the other hand, have this stabilizing charges fixed (chemically bounded). Hence, they are inherently doped.

The amount of coupling between electronic charges and excess ionic charges in OMIECs can be modulated by an applied bias when coupled through an electrolyte [18]. This is the basic principle of OECTs, and it will be further discussed in Section 2.3.

2. BACKGROUND

2.2.1.2 Electronic transport

Electronic charge transport mechanisms present in OMIECs are thermally-activated hopping and band-like transport, as represented in Figure 2.7, which are not different from other conjugated polymers. The former, as its name suggests, is driven by thermal energy and it is limited by the degree of structural disorder, where the weakly-bond electrons in delocalized π -orbital move along an adjacent π -orbital within the length of the conjugated polymer, or even between molecules where there is sufficient π - π overlapping. This mechanism is predominant for low electronic charge carrier density and the low density of accessible hopping states. Hopping-like transport results in low mobility and electrical conductivity [18].

The band-like transport, on the other hand, occurs normally in OMIECs with increasing doping levels, where the activation energy of charge hopping decreases and carrier mobility increases, leading to diffuse band-like charge transport and it is shown within the polymer-stacking [19].

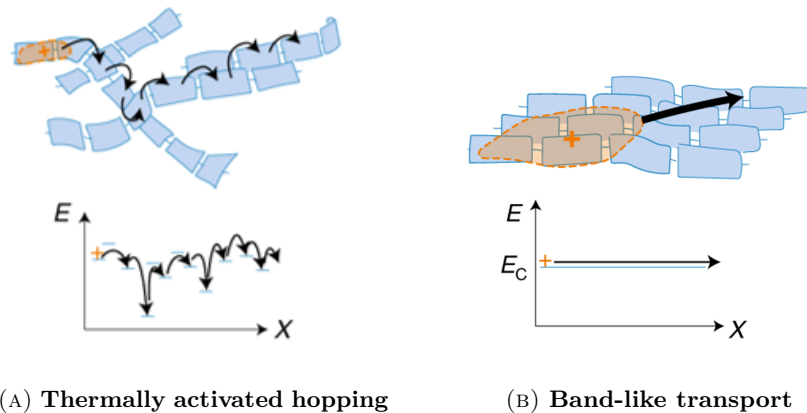


FIGURE 2.7: Schematic representation of electronic charge transport mechanisms: A) Thermally-activated hopping transport and B) band-like transport, where the electronic charge carrier is relatively localized and delocalized, respectively. Extracted from reference [18].

2.2.1.3 Ionic transport

Although transport of charged anions and cations can be seen in analogy to electrons and holes, it is a more complex process, since ions can be “*multi-valent, and form pairs and larger clusters; moreover, they are sensitive to solvent and solvation*” [18].

Ion transport is unipolar for dry OMIECs of type I, III and V, since they are fixed on a polyelectrolyte, which is not the case for type II, IV and VI, where both anions and cations are mobile. OMIECs in contact with an electrolyte swell, which allows the penetration of excess ions from the electrolyte, therefore both mobile anions and cations would contribute to ion transport to ensure electroneutrality.

Then two types of ionic charge transport can be differentiated: ion hopping and vehicular solvated-ion transport. In dry or minimally hydrated OMIECs, only ion

hopping assisted by segmental motion of the OMIEC side chains or backbone occurs, as shown in Figure 2.8A; whereas, when the OMIEC is in contact with solvent or liquid electrolyte, both mechanisms are present but predominantly solvated ion vehicle transport. For instance, in water-based electrolytes, proton diffusion occurs via the Grotthuss mechanism, where protons in the water molecules diffuse within the neighboring molecules, this implies a transfer of an ionic effect through the hydrogen-bonded network, as shown in Figure 2.8B.

Finally, due to the existing ionic-electronic coupling, both ionic and electronic transport in OECTs and other OMIEC-electrolyte based applications, are not independent but are rather complex and needs to consider side effects, such as hydration and electrolyte swelling [18], which will be further discuss in section 2.3.

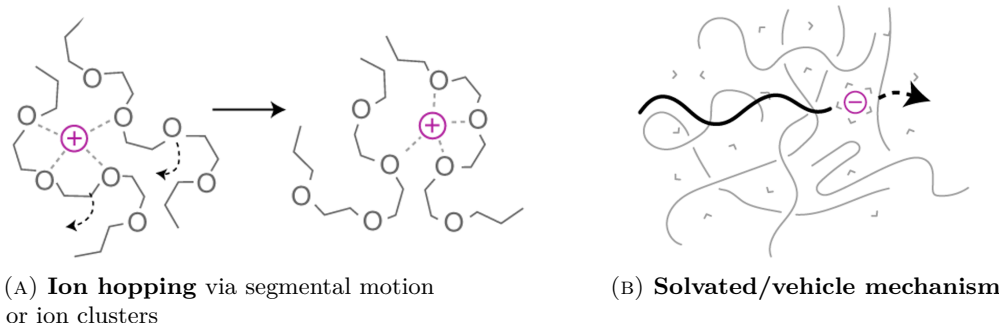


FIGURE 2.8: Schematic representation of ionic charge transport mechanisms: A) Ion hopping via segmented motion and B) vehicular solvated-ion transport. Extracted from reference [18].

2.3 Organic Electrochemical Transistors

Organic Electrochemical Transistors consists of metallic source, drain and gate electrodes, an organic conjugated polymer channel (specifically an OMIEC as described in previous sections) and an electrolyte that couples channel and gate, as represented in Figure 2.10A. OECTs are devices that have received increasingly attention due to their mechanically compliance, biocompatibility, and are sensitive to biochemical modules [20].

2.3.1 Device Physics

Although the structure of OECTs is different from conventional metal-oxide-semiconductor field-effect transistors (MOSFETs), the basic understanding of the latter can give us a clear idea of how OECTs operate. Unlike MOSFETs, OECTs are coupled with an electrolyte rather than an insulator, as seen in Figure 2.9. So, when applying a gate voltage, instead of polarizing the dipoles in the insulator, creating a field that causes accumulation of carriers at the interface of the semiconductor/insulator as it happens in a MOSFET, in an OECT, the gate voltage drives ions to penetrate the

2. BACKGROUND

bulk of the channel, therefore accumulation of carriers will happen throughout the whole volume of the OMIEC film. This mechanism explains the large gate-channel capacitance in these devices compared to MOSFETs, and why the drain current takes into account a volumetric capacitance [21].

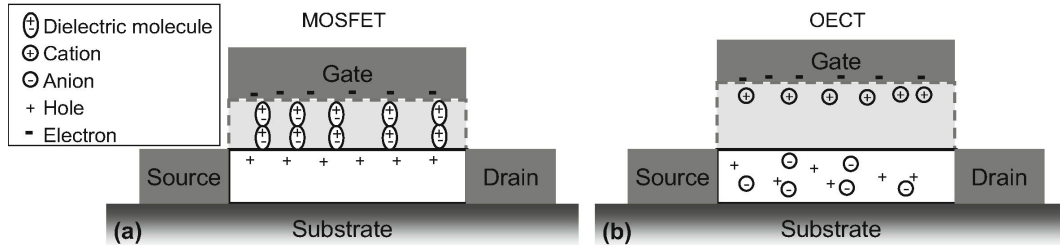


FIGURE 2.9: Comparison of p-type A) MOSFET and B) OECT, where the light-gray region represents an insulator and a electrolyte, respectively. Extracted from reference [21]

Bernards and Malliaras implemented a model based on a p-type depletion-mode OECT (based on PEDOT:PSS since it is widely fabricated and investigated, further discussion in the following section). The model divides the behavior of the OECT into an electronic (source-channel-gate structure) and an ionic circuit (gate-electrolyte-channel structure). The electronic circuit is treated as a *variable* resistor therefore it is modeled using Ohm's law. Its variability lies on the fact that upon the application of a positive gate voltage, de-doping of the semiconductor occurs, analogous to the compensation doping of silicon, cations from the electrolyte penetrate the polymer, compensating one acceptor. Meanwhile, the ionic circuit consists of a resistor that represents the flow of ions in the electrolyte, in series with a capacitor, representing the storage of ions in the channel as shown in Figure 2.10B [1][22].

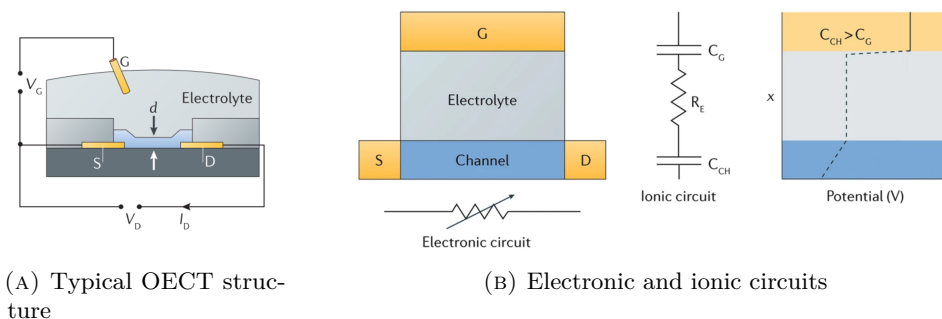


FIGURE 2.10: A) Typical structure of an organic electrochemical transistor (OECT). B) (Left) Electronic circuit modelled as a resistor with a variable resistance. (Right) Ionic circuit consisting of channel (C_{CH}) and gate (C_G) capacitors, coupled with a resistor corresponding to the electrolyte (R_E). Extracted from reference [1].

2.3.2 Operation Modes

Analogous to conventional MOSFETs, depending on whether the device needs a gate potential to turn it ON, it will describe two operation modes: depletion and enhancement (the latter commonly named as accumulation for OECTs). These operation modes have a strict relationship to the channel material.

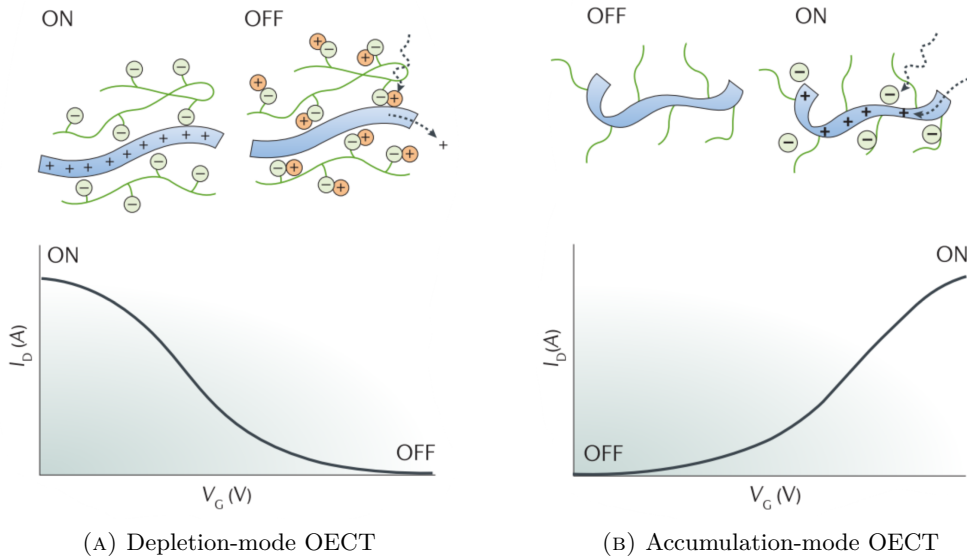


FIGURE 2.11: (A) Transfer curve showing depletion-mode operation of a p-type OECT with a conducting polymer channel. (B) Transfer curve showing accumulation-mode operation of a p-type OECT with a semiconducting polymer channel. Images extracted from reference [1].

As seen in Figure 2.11A and B), the polymer can be intrinsically doped (conductive) or undoped (insulating). In the first scenario, the OMIEC already possesses anions which have had induced charges within its backbone, therefore it needs the injection of cations to counteract this effect, hence turn off the device. The opposite scenario is presented for an insulating polymer channel, a zero-gate biased OECT would have no charges in its backbone hence the device will be in OFF state, it will need the application of a gate voltage to drive anions into the polymer and induce charges.

2.3.2.1 Standard material for depletion-mode OECTs

Poly(3,4-ethylenedioxythiophene) poly(styrene-sulfonate) (PEDOT:PSS) is a “*degenerately doped*” [22] or conductive polymer that is widely used in multiple applications in organic electronics. Classified as type I OMIEC, as seen in Figure 2.6, it is a blend between a conjugated polymer (PEDOT) and a polyelectrolyte (PSS), the latter possesses chemically linked ions and serves as a polymeric acid template to allow dispersable suspensions [18].

2. BACKGROUND

Due to its commercial availability, operational stability, and relatively high performance, PEDOT:PSS became a standard material for p-type OECTs. Its main drawback lays in its depletion-mode operation, since, as explained in the previous section, requires power to turn off.

With the aim of minimizing power consumption, there is a special interest to fabricate accumulation-mode devices with high performance [2][14][23][24]. This type of devices have the advantage of dissipating less static power when the device is not operated, due to low OFF current [15].

2.3.2.2 Prospective materials for accumulation-mode OECTs

PEDOT:PSS was not descarted as a possible accumulation-mode OECT, Keene et al. used a series of amines to de-dope PEDOT:PSS and obtain OECTs with negative turn-on voltages [24]. However, synthetically modifying PEDOT:PSS in a controlled manner remains complicated. Parallel to these efforts, the design of new semiconducting polymers with the aim of not only having acummulation-mode OECTs but enhancing performance is also studied. Nielsen et al. reported a series of semiconducting polymers with Triethylene glycol (TEG) side chains with good performance. Among the five thiophene- and benzodithiophene-based polymers, they found out that the backbone consisted of 2,2'-bithiophene polymerized with other thiophene molecule (g2T-T), as seen in Figure 2.12, showing the highest performance [2].

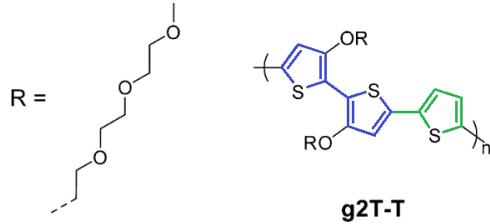


FIGURE 2.12: Chemical structure of polymer with backbone g2T-T, R representing the side chain. Extracted from reference [2]

Moser et al. took the same backbone and studied the impact of the length of the ethylene glycol (EG) side chain on the performance of OECTs. They reported that reducing chain length maximized both the capacitance and mobility; nonetheless, it was unfavorable for ion-polymer interaction. Finally, they suggested an optimum-side-chain length of 3 monomers (over 2, 4 and 6 monomers), demonstrating that an OECT with 3-(2-(2-(2-methoxyethoxy)ethoxy)thiophene (p(g3T2-T)) has a turn-on voltage close to zero and better performance compared to other thiophene-based species (as seen in Figure 2.13), even better than PEDOT:PSS OECTs [25].

The structural tuning of this polymer was thought to have a backbone that warrants reversibility during electrochemical redox reactions and good electronic transport, meanwhile having side chains that enable its stability in aqueous electrolytes and efficient transport of ionic and electronic charge carrier [26].

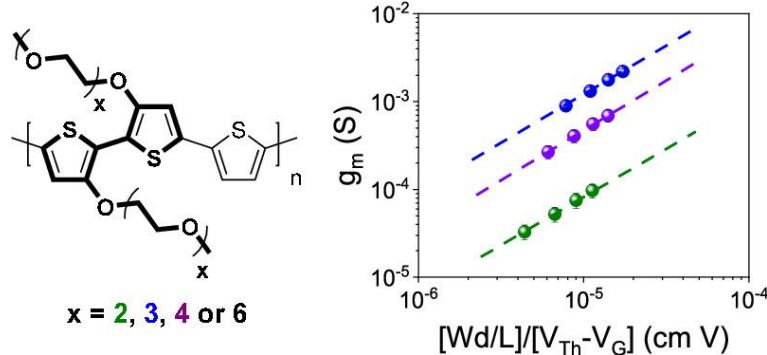


FIGURE 2.13: (Left) Chemical structure of the repeat units for p(gxT2-T). (Right) Transconductance vs channel geometry and operating parameters of p(gxT2-T) for $x = 2, 3$ and 4 . Extracted from reference [25].

Under the classification shown in Figure 2.6, p(g3T2-T) can be identified as a type VI OMIEC that comprises a conjugated polymer with ions introduced as **free species** whereas PEDOT:PSS' ions are **chemically linked** to the polyelectrode (PSS). This structural characteristic make p(g3T2-T) display larger magnitudes of ionic-electronic coupling and volumetric capacitance than biphasic OMIECs (such as PEDOT:PSS) [18] and at the same time will be important for understanding the challenges on having a stable OECT, further discussion in Section 2.3.4.

2.3.3 Important Figures of Merit

2.3.3.1 Transconductance

Transconductance is considered as the most important parameter to measure any transistor's amplification capability, calculated as the first-order derivative of the output current (drain current) with respect to the input voltage (gate-source voltage): $g_m = \partial I_D / \partial V_{GS}$. Bernards and Malliaras calculated this parameter from their implementation of a mathematical model for depletion-mode p-type OECTs [22], as previously seen in Section 2.3.1. Including also n-type, the following equation expresses the transconductance:

$$g_m = \frac{Wd}{L} \mu C^* |(V_{th} - V_G)|, \quad (2.1)$$

where W , L and d are the channel width, length and thickness, respectively, μC^* product, the gate voltage (V_G) and threshold voltage (V_{th}), which will be discussed in the next subsections.

Commonly, the maximum value of transconductance is reported ($g_{m,max}$), which falls into the saturation regime. Inal et al. reported the maximum transconductance of various channel materials at different device geometry parameters using a Ag/AgCl pellet as reference/gate electrode and 0.1M NaCl as electrolyte, showing OECTs with polymerized-g2T-backbones, the best performances, within the range of 1 to 30 mS, depending on the geometry (Figure 2.14A) [23].

2. BACKGROUND

2.3.3.2 μC^* product

μC^* is the most important parameter for benchmarking OEET channel materials, that represents both ionic and electronic transport properties [23]. It is the product of two important parameters, μ , the electronic mobility, and C^* , the volumetric capacitance, the latter encloses the ion penetration, transport, and storage ability of the OMIEC film.

Along with the transconductance, Inal et al. extracted the values of μC^* from the calculating the linear slope of the maximum transconductance and channel geometry (Figure 2.14A), following Equation 2.1. She correlated her results with the independent calculation of both parameters, showing again polymerized-g2T-backbones with the highest value of $261 \pm 29 F cm^{-1} V^{-1} s^{-1}$, and among the materials that have closest 1:1 relation for both methods of calculation the μC^* product (Figure 2.14B) [23].

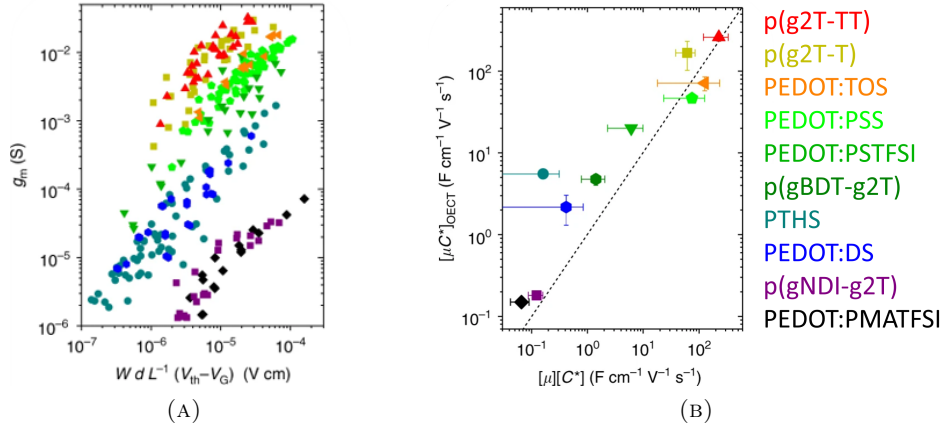


FIGURE 2.14: A) Plot of μC^* product calculated by the linear slope between transconductance and channel geometry. B) Calculated slope from A) in function of the product of independent determination of μ and C^* , dotted line represents the 1:1 relation between both methods of calculation. Extracted from reference [23].

The independent calculation of μ is yet difficult due to the presence of ionic species, normally calculated in transient regimes, taking advantage of ions' lower mobility, which is out of the scope of this work. Among the method to calculate C^* , performing Electrochemical Impedance Spectroscopy (EIS) is a straightforward one, and by using Equation 2.2 to calculate the capacitance, at low frequency ranges where the capacitance should describe a plateau, since the modulation of AC is slow enough to fully populate the OMIEC with ions. Finally, the value is divided the calculated capacitance by the film volume to obtain C^* [27].

$$C = \frac{1}{2\pi \cdot f \cdot |Z^{img}|}, \quad (2.2)$$

where $Z^{img}(\Omega)$ is the imaginary part of the impedance and f is the frequency (Hz).

The calculation of this capacitance is under a fixed-gate biased condition, it is important to remember that the modulation of the degree of electrochemical doping in OECTs with an applied biased, will manifest a potential-dependent capacitance (C) [23].

2.3.3.3 Threshold voltage

From the steady-state characteristics of an OECT, specifically the transfer characteristics (I_D vs V_{GS}), one can calculate not only the transconductance but also the ON/OFF ratio and the threshold voltage (V_{th}). The latter can be determined by plotting the square root of I_D as a function of V_{GS} and extrapolate the linear portion of the slope, where the intersection with the x-axis will give this parameter [27].

In OECTs, it represents the “film’s readiness for ion penetration” [27]. Controlling and/or shifting this parameter is wished, specially to integrate transistors and meet any circuit requirement and control operation, noise margins, and power consumption.

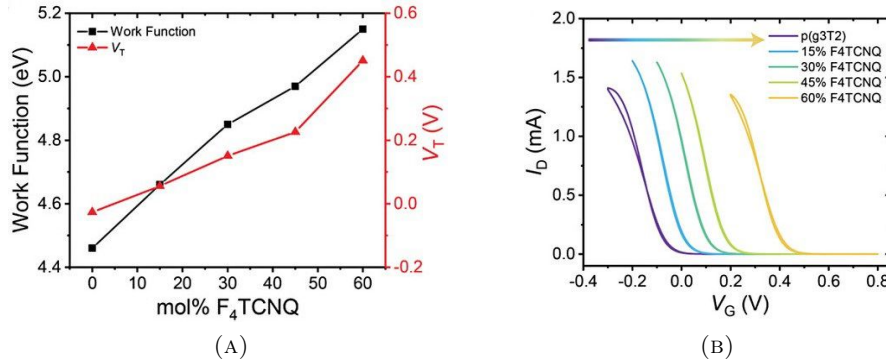


FIGURE 2.15: Controlling OECT threshold voltage by chemical doping of p(g3T2-T) gate electrode with $F_4\text{TCNQ}$. A) Plot of threshold voltage and gate work function for doped gates of different dopant concentrations. B) Transfer curves of p(g3T2-T) channel OECT with p(g3T2) gates of various $F_4\text{TCNQ}$ dopant concentrations. . Extracted from reference [3].

The chemically de-doping of PEDOT:PSS by Keene et al. described in previous sections, is also an approach to shift the threshold voltage, until reaching negative values, characteristic for accumulation-mode OECTs [24]. Tan et al., on the other hand, explored a different approach, rather than modifying the doping level of the channel, they tuned the doping level of the gate to shift the threshold voltage. They used p(g3T2-T) and obtained a 400mV change with 60% mol ratio of 2,3,5,6-Tetrafluoro-7,7,8,8-tetracyanoquinodimethane ($F_4\text{TCNQ}$) dopant, as seen in Figure 2.15. The advantage over this approach is i) protecting the material from oxidation with air, since the Fermi level is brought towards the highest occupied molecular orbital (HOMO), and ii) no interference with the channel which helps to leave the transconductance unaffected [3].

2. BACKGROUND

2.3.4 Side Reactions

2.3.4.1 Water uptake and swelling

Water-based electrolytes are widely used, and even in the pursue of solid-state OECTs, precursors have a certain degree of water content [4][28], hence, side reactions of OMIECs upon water contact are inevitable and therefore, studies to understand the impact are necessary. Water uptake in OMIECs cause their increase of mass (swelling) and change in morphology. Water uptake happens since OMIECs will need to compensate their intrinsic doping. Therefore, “*the effect of doping-induced hydration on the OMIEC morphology must be taken into account when designing OECTs*” [29].

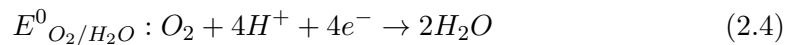
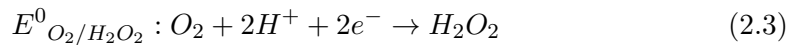
Savva et al. studied the influence of water on the performance of PEDOT:PSS OECT, the water uptake led to 10-13% mass increase under non-biased conditions. As the concentration of water decreased (NaCl_{aq} 10 mM, 100mM, 1M, and 6M) ionic charging got faster; however, the fastest response time is not achieved by the highest salt concentration but rather NaCl_{aq} 1 M. This due to attractive forces between counter ions which hinders the drift of anions, hence delays the ion injection from the electrolyte [30].

In another study, Savva et al. showed that a certain level of hydration is necessary for facile ionic transport, but can negatively impact electronic charge transport, in glycol-based side chains [29], commonly used in accumulation-mode OECTs and where ionic transport is already enhanced by side-chain engineering [26].

2.3.4.2 Oxygen Reduction Reaction (ORR)

Oxygen Reduction Reaction is a common undesirable side reaction at environmental conditions, specially among devices fabricated with polymers with low ionization potential (IPs). The utilization of OMIECs with low IP are frequent in accumulation-mode OECTs.

The ORR is a non-capacitive faradaic reaction between the OMIEC and molecular oxygen, where electron-transfer occurs. The reaction yields either hydrogen peroxide (H_2O_2) or water (H_2O), as described in 2.3 and 2.4, or oxidation (p-doping) of the OMIEC that acts as the catalyst [15].



As seen in Figure 2.16, η_1 and η_2 represent free energy difference between reactants and the reaction products H_2O_2 and H_2O , respectively. If this free energy is negative, the reaction is endergonic (the opposite is exergonic), and needs energy to be driven. PEDOT:PSS and p(g3T2-T) exhibit exergonic reactions. For instance, a polymer with higher IP ($> 4.9\text{eV}$) would be needed to prevent oxygen peroxide to form.

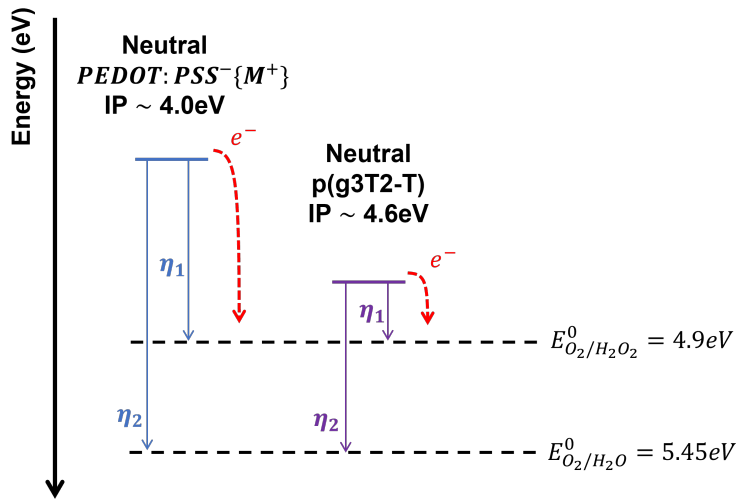


FIGURE 2.16: Simplified mechanism of two- and four-electron Oxygen Reduction Reactions with neutral states of OMIECs: p(g3T2-T) and PEDOT:PSS. The free energy difference between reactant and the reaction products is represented by η . Image adapted from reference [15], where values are defined from cyclic voltammetry measurements using Ag/AgCl as reference electrode and NaCl as electrolyte.

Chapter 3

Experimental Methods

3.1 Materials

All reactives were purchased from commercial suppliers.

- Chromium etchant: Standard, Sigma Aldrich
- Gold etchant: Standard, Sigma Aldrich HHPAA (2-Hydroxy-4'-(2-hydroxyethoxy)-2-methylpropiophenone), 98%, Sigma Aldrich
- Developer: AZ 726 MIF Developer, Merck performance Materials GmbH
- EG: Ethylene glycol, \geq 95%, Sigma Aldrich
- [EMIM][EtSO₄]: (1-Ethyl-3-methylimidazolium ethyl sulfate), \geq 95%, Sigma Aldrich
- MBBAm: (N,N'-Methylenebisacrylamide), 99%, Sigma Aldrich
- NIPAm: (N-Isopropylacrylamide), 97%, Alfa Aesar
- Sacrificial Layer 1: Sacrificial Layer 1 (SL1), Orthogonal Inc
- Photoresist: AZ 1518 Photoresist, Merck Performance Materials GmbH & Microchemical GmbH
- Photoresist for undoped species: NLOF 2020, commercial negative-tone photoresist, Microchemical
- Orthogonal Photoresist for doped species: OSCoR 4020 Photoresist, Orthogonal Inc.
- Developer for SL1: Developer HF 7300, Orthogonal Inc.
- Orthogonal Developer for OSCor 4020: Orthogonal Developer 103a, Orthogonal Inc.

3. EXPERIMENTAL METHODS

- Orthogonal Stripper: Orthogonal Stripper 900, Orthogonal Inc.
- p(g3T2-T): 3-(2-(2-methoxyethoxy)ethoxy)ethoxythiophene
- Dopants: 1,3,4,5,7,8-hexafluorotetracyanonaphthoquinodimethane (F_6TCNNQ) and 1,3,4,5-tetrafluorotetracyanonaphthoquinodimethane (F_4TCNQ)
- Adhesion promoter: Silane A174 (3-(Trimethoxysilyl)propyl methacrylate), TCI

3.2 Equipment

- Baking: All baking steps were carried out on a Stuart SD160 digital hotplate (Stuart Equipment, UK).
- Electrical characterization (ambient): Device characterization under ambient conditions was performed on a Everbeing C-6 Probe Station (Everbeing Int'l Corp., Taiwan), connected to a Keithley 4200-SCS Semiconductor Characterisation System (Keithley Instruments, USA).
- Electrical characterization (glovebox): Device characterisation was performed in a nitrogen-filled glovebox. Probing needles were connected to two Keithley 236 Source Measure Units (Keithley Instruments, USA).
- Cyclic voltammetry and Impedance measurements: Measurements were carried out by using a Metrohm Autolab PGSTAT302N potentiostat/galvanostat (Metrohm AG, Switzerland).
- Micrographs: Micrographs were taken on a Nikon Eclipse LV100ND microscope, equipped with a DS-Fi2 camera (Nikon, Japan).
- Photolithography: Photolithography was carried out on a SÜSS Microtec MJB4 maskaligner system (SÜSS Microtec AG, Germany).
- Photomasks: Photomasks were custom made by Compugraphics Jena in a 4-inch format (soda-lime glass covered with chromium) and held several mask designs (Compugraphics Jena GmbH, Germany).
- Plasma cleaning: O_2 -plasma cleaning was performed by using a Harrick PDC-002 plasma cleaner (Harrick Plasma, USA), connected to a Leybold Heraeus Combitron CM 330 Vacuum Gauge Controller (Leybold GmbH, Germany).
- Plasma etching: O_2 -plasma etching was performed by using a Diener electronic ATTO plasma cleaner (Diener electronic GmbH & Co. KG, Germany).
- Profilometry: Profilometry was performed on a Veeco Dektak 150 surface profiler (Veeco Instruments Inc., USA).

- Film resistance measurements: The film resistance was measured using a linear four-point probe system (Lucas four-point probe connector) connected to a multimeter (Keithley 2010 Multimeter).
- Transmittance and Reflectance measurements: Measurements were performed with UV-Visible-NearInfraRed Spectroscopy on a SolidSpec-3700 UV-Vis-NIR spectrometer using an integral sphere from Shimadzu.
- Energy of HOMO/HBEC cutoff measurements: Measurements were done using Ultraviolet Photoelectron Spectroscopy (UPS) on a PHOIBOS 100 from Specs, a Helium plasma discharge lamp (UVS10/35, Specs).
- Spincoating: Samples were coated with a SAWATEC SM-180-BT spincoater (SAWATEC AG, Switzerland).

3.3 Software

- Data processing: All data was processed by customized scripts written in Python. Files import and manipulation was done by using OS [31] and CSV [32] modules. Mathematical computations (e.g. fits, integration) were carried out by employing the NumPy [33], SciPy [34], and PeakDetect [35] libraries. Visualisations were performed using the Matplotlib library [36]. All is compiled in the following GitHub Repository: **marivelasco25/Thesis.git**.
- Electrical characterisation: Measurements were performed by controlling SMUs through the in-house developed SweepMe! software (<https://sweep-me.net/>).
- Profilometry: Profilometry was performed by using the Dektak software (Veeco Instruments Inc., USA).
- Cyclic voltammetry: Measurements were performed by using the NOVA software (Metrohm AG, Switzerland). Parameters were fixed and are described in the following table:

TABLE 3.1: Cyclic Voltammetry parameters.

Parameter	Value
Start/Stop potential	0 V
Upper vertex potential	1 V
Lower vertex potential	-1 V
Number of scans	10
Scan rate	0.1 V/s

- Impedance measurements: Measurements were performed by using the NOVA software (Metrohm AG, Switzerland) in potentiostatic mode. Parameters were fixed and are described in the following table:

3. EXPERIMENTAL METHODS

TABLE 3.2: Electrochemical Impedance Spectroscopy parameters.

Parameter	Value
Initial frequency	10^5 Hz
Final frequency	10^{-1} Hz
Frequencies per decade	10
Amplitude (V_{RMS})	0.01 V

3.4 Experimental Procedures

All fabrication steps were performed under standard cleanroom conditions.

3.4.1 Preparation of Films

Dynamic spin-coating of p(g3T2-T). Unlike reference [3], in which drop cast is used to deposit undoped and doped p(g3T2-T), in order to perform photolithography and being able to do a miniaturization process, homogeneous films are needed. Dynamic spin-coating was previously established by BioSens group members at IAPP, due to the high volatility of p(g3T2-T) solvent: chloroform. Substrates were cleaned using subsequent steps of ultrasonic bath with acetone for 15 minutes, IPA rinsing, N₂-drying and O₂-plasma etching for 5 min (0.3 mbar). Then, 70 μ L of 10 mg/mL of p(g3T2-T) mixed at 60°C for 20 minutes, was dynamic-spin-coated at 3000 RPM for 60s, to yield approximately 70nm-thick films. Dry sample at 80°C.

Dynamic spin-coating of F₄TCNQ dopant. Different doping levels of p(g3T2-T) were achieved by dynamic spin-coating 140 μ L of dopants at different concentrations (5, 10 and 20 mg/mL), previously mixed in acetonitrile at 60°C for 20 minutes. Dry sample at 80°C.

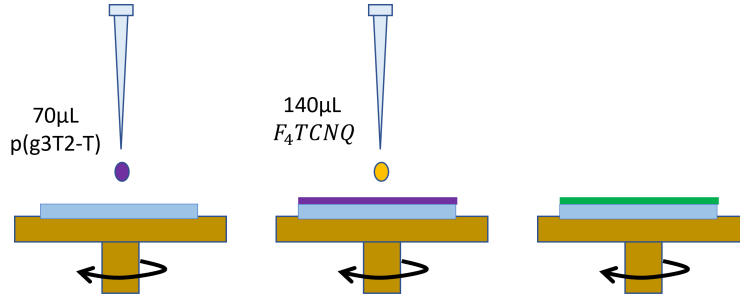


FIGURE 3.1: Dynamic spin-coating process to obtain undoped and doped films of p(g3T2-T).

3.4.2 Doping Characterization of Films

UV-Vis-NIR Spectroscopy. After the preparation of the films, transmittance (T) and reflectance (R) was measured using the UV-Vis-NIR Spectrometer in the range of 285 to 1600 nm, and slit width of 5.0 nm. Then absorption (A) was calculated via

$$A = 1 - T - R, \quad (3.1)$$

and normalized with respect to the incoming light [37]. Additional measurements were taken, after some days of storage under ambient conditions to check its stability on air.

Ultraviolet Photoelectron Spectroscopy. After the preparation of the films, the energy of the highest occupied molecular orbital cutoff (E_{HOMO}) and the high binding energy cutoff E_{HBEC} was measuring using UPS. The pressure in the chamber during measurements was about $5 \cdot 10^{-9}$ mbar, while the base pressure is in the range of $10 \cdot 10^{-10}$ mbar. The workfunction (WF) and ionization energy (IE) are calculated by using the following equations:

$$WF = h\nu - E_{HBEC} \quad [eV], \quad (3.2)$$

$$IE = h\nu - (E_{HBEC} - E_{HOMO}) \quad [eV], \quad (3.3)$$

where $h\nu = 21.22\text{eV}$, the main He I excitation line of the Helium plasma discharge lamp [38].

Profilometer. The films were scratched 4 times to remove part of material, and measure the cavity depth to obtain the film thickness.

Four-point probe. Sheet resistance was calculated via

$$R_S = \frac{\pi}{\ln(2)} R = 4,53R \quad [\Omega/sq], \quad (3.4)$$

where R is the resistance measured with the four-point probe setup and resistivity was calculated using the following equation:

$$\rho = R_s t \quad [\Omega.cm], \quad (3.5)$$

3.4.3 Fabrication of Organic Electrochemical Transistors

3.4.3.1 Influence of Doping OECT Channel

Photolithographically patterned substrates with gold contacts for source, drain and gate were obtained following references [4][39], described in Figure 3.2.

Then p(g3T2-T) films were deposited following the procedure described in the previous section. The patterning of doped-p(g3T2-T) channel follows a similar

3. EXPERIMENTAL METHODS

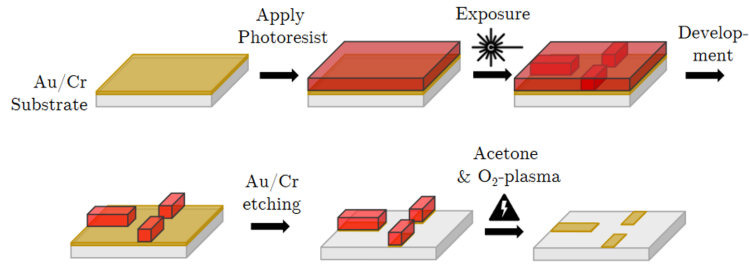


FIGURE 3.2: Visualization of the workflow for Au-contacts patterning. Image modified based on reference [39].

procedure from references [4][39], where PEDOT:PSS is being used, with some modifications in the exposure and developing times. The patterning of undoped-p(g3T2-T) samples, on the other hand, follows a different protocol, the addition of a sacrificial layer is needed to ensure cross-linking. Both processes are described in the following:

Patterning undoped-p(g3T2-T). Patterning of the p(g3T2-T) was achieved with photolithography, as shown in Figure 3.3. First, a fluoropolymer Sacrificial Layer 1 (SL1) was spin coated at 6000 RPM for 60 s, followed by a baking step for 180 s at 113°C. Before the deposition of photoresist, a O₂ plasma cleaning step was applied for 60 s to promote adhesion. Then, NLOF 2020 photoresist was spin coated at 3000 RPM for 60 s and baked for another 60 s at 113°C. Exposure of negative resist was performed for 12 s by shadowing all areas except the ones of interest. After post-baking for 60 s at 113°C, NLOF was developed by rinsing the sample in AZ MIF 726 for 20 s and wash off in DI water (carried out extra times if necessary). Next, SL1 was developed using HF 7300 developer for 45 s and spin rinsed at 3000 RPM (carried out extra times if necessary). Excess of p(g3T2-T) was removed by O₂-plasma etching for 180 s. The sample was placed in Orthogonal Stripper 900 overnight at room temperature, to complete the removal. Finally, ultrasonication in acetone was added for 15 min the next day.

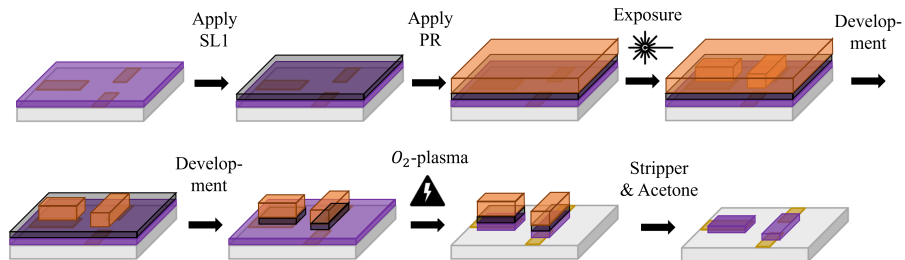


FIGURE 3.3: Visualization of the workflow for patterning undoped p(g3T2-T).

3.4. Experimental Procedures

Patterning doped-p(g3T2-T). Patterning of the doped-p(g3T2-T) was achieved with photolithography, as shown in Figure 3.4. First, the orthogonal photoresist OSCoR 4020 was spin coated at 3000 RPM for 60 s and baked for another 60 s at 103°C. Exposure of negative resist was performed for 20 s with shadowing all areas except the ones of interest, one extra cycle was added if using higher dopant concentration (10 mg/mL). After post-baking for 60 s at 103°C, OSCoR was developed using Orthogonal Developer 103a for 45 s and spin rinsed at 3000 RPM for 60 s (carried out extra times if necessary). Excess of doped-p(g3T2-T) was removed by O₂-plasma etching for 180 s. The sample was placed in Orthogonal Stripper 900 overnight at room temperature.

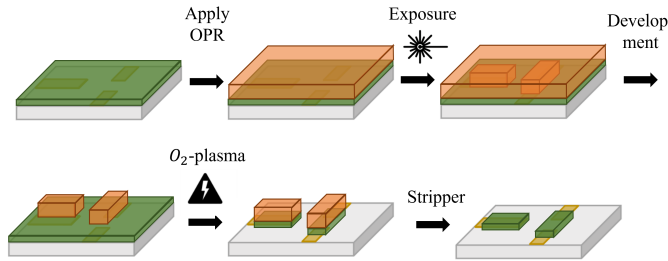


FIGURE 3.4: Visualization of the workflow for patterning doped p(g3T2-T).

OECT with undoped- and doped-p(g3T2-T) channel. A solid-state electrolyte precursor was prepared, as described in Table 3.3, and 20 μL were dropcasted to the patterned samples (undoped and doped) covering all 14 devices in the sample. Finally, a Ag/AgCl pellet was installed and used as gate (Figure 3.5). Transfer characteristics were measured under ambient conditions with different source-drain voltages ($V_{DS} = -0.1, -0.2, -0.5V$).

TABLE 3.3: Composition of the solid-state electrolyte [4].

Component	Amount
H ₂ O	1.0 mL
[EMIM][EtSO ₄]	1.5 mL
MBBAm	20 mg
NIPAm	750 mg
HHPAA	200 mg

3.4.3.2 Stability on Air of p(g3T2-T)

In this subsection, the stability of undoped and doped samples of p(g3T2-T) (doped with F₆T CNNQ, following same procedure described in subsection 3.4.1) in N₂ and ambient conditions were tested at different stages of the photolithography process by measuring the channel conductivity under a fixed biased drain-source voltage.

3. EXPERIMENTAL METHODS

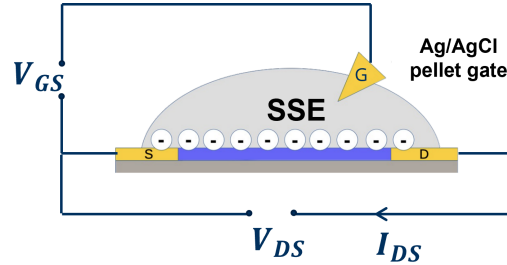


FIGURE 3.5: Experimental setup to measure threshold voltage shift under ambient conditions.

Channel conductivity measurements. Undoped-p(g3T2-T) sample was measured in N₂ then ambient conditions immediately after spin-coating onto substrate with patterned gold contacts. Then, sample was measured after patterning process (as described in previous section). Finally, upon drop-casting solid-state electrolyte precursor. The doped-p(g3T2-T) channel was measured after patterning and upon dropcasting solid-state electrolyte precursor.

3.4.3.3 Reverse Oxidation of Undoped-p(g3T2-T)

By electrochemical dedoping. Undoped-p(g3T2-T) samples onto patterned-gold-contacts substrates were prepared. The solid-state-electrolyte precursor was dropcast onto the 14 devices, one device source-drain was negatively-biased and applied a positive gate voltage. Channel conductivity was monitored. Finally, other devices on the sample were measured to detect any effect of the process.

By heating. An undoped-p(g3T2-T) solid-OECT, whose fabrication will be described in the following subsection (3.4.3.4), was exposed to ambient conditions, devices were clearly oxidized. The sample was placed on a hot plate at 120°C, brought back to glovebox, and measured the following day.

3.4.3.4 Solid-OECTs using Undoped-p(g3T2-T)

After following the patterning steps for undoped-(pg3T2-T) from Subsection 4.5. Three different methods of applying the solid-state electrolyte precursor were tested. Then, transfer characteristics at $V_{DS}=-0.1V$ at a scanning rate of 0.083 V/s were measured. Cyclic voltammetry and electrochemical impedance spectroscopy was performed by short-circuiting source and drain to probe between channel and gate, parameters were fixed as described in Section 3.3, measurements were taken one day after the fabrication.

OECT with dropcasted Solid-State Electrolyte. Solid-state electrolyte precursor was dropcasted and then exposed for 2 cycles of 60 s in mask aligner, as shown in Figure 3.6A.

3.4. Experimental Procedures

OECT with photopatternable Solid-State Electrolyte. First, the application of an adhesion promoter was used, composed by reactants from Table 3.4, the sample was covered in Petri dish at 50°C, then rinse very thoroughly with ethanol and dried for at least 10 min at 100°C on hot plate. Composition and application steps of adhesion promoter was previously defined by Biosens group members at IAPP. Solid-state-electrolyte precursor was dropcasted, then a Teflon foil was placed on top to avoid contact with mask that will shadow all areas except the ones of interest in the negative resist, exposed for 2 cycles of 60 s in mask aligner, and blown off with a N₂ gun, as shown in Figure 3.6B, following references [4][39].

TABLE 3.4: Composition of adhesion promoter.

Component	Amount
SilaneA174	30 μ L
Ethanol	3mL
Acetic acid	60 μ L

OECT with inkjet-printed Solid-State Electrolyte. First, the application of an adhesion promoter as described previously. Then, the solid-state-electrolyte precursor was ink-jet printed and expose for 2 cycles of 60 s in mask aligner, parameters and procedure for ink-jet printing was previously established by members of BioSens group at IAPP, as shown in Figure 3.6C.

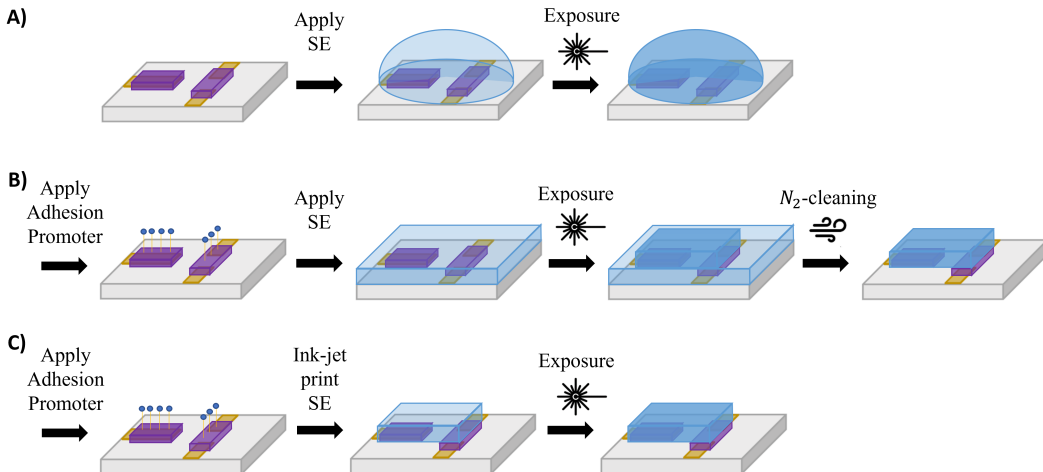


FIGURE 3.6: Visualization of the workflow for solid-OECT fabrication with undoped p(g3T2-T) by A) dropcasting SSE, B) photopatterning SSE, C) ink-jet printing SSE.

3.4.3.5 Solid-OECTs using Doped-p(g3T2-T)

OECT with inkjet-printed Solid-State Electrolyte. After the deposition of films and dopant (F₆T CNNQ), films were stored in glovebox over the weekend to

3. EXPERIMENTAL METHODS

let dopants soak and dry. Then, the patterning steps for doped-(pg3T2-T) from Subsection 4.5 were followed with no extra cycles in exposure times. Solid-state-electrolyte precursor was ink-jet printed as described in the previous Subsection. Then, transfer characteristics at $V_{DS}=-0.1V$ at a scanning rate of 0.083 V/s were measured. Cyclic voltammetry and electrochemical impedance spectroscopy were performed by short-circuiting source and drain to probe between channel and gate, parameters were fixed as described in section 3.3, measurements were taken one day after the fabrication.

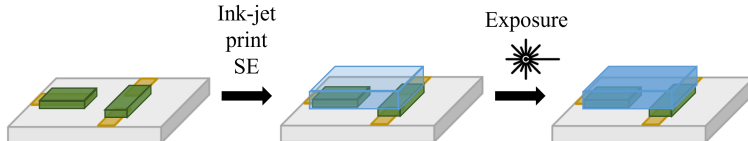


FIGURE 3.7: Visualization of the workflow for solid-OECT fabrication with doped p(g3T2-T) by ink-jet printing SSE.

Chapter 4

Results and Discussion

4.1 Doping Characterization

Upon increase of the dopant concentration that is deposited and bake on top of the p(g3T2-T) film, the reflection hue, as observed in Figure 4.1 shift towards more yellowish colors.

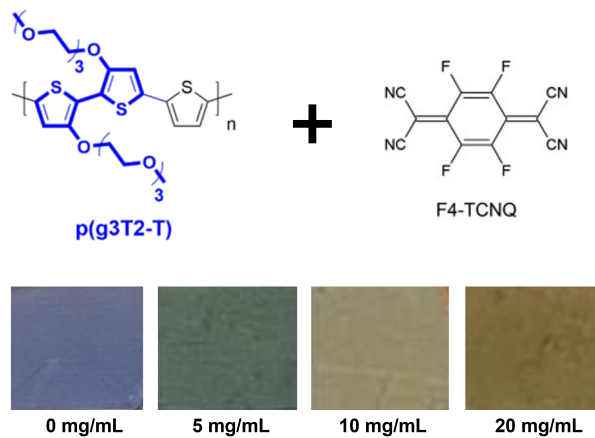


FIGURE 4.1: (Top) Chemical structure of p(g3T2-T) and F₄TCNQ dopant. (Bottom) Color change upon increasing dopant concentration from 0 to 20 mg/mL.

4.1.1 Absorbance and Dopants Diffusion

The visible color hue shift can be described quasi-quantitatively by the absorbance spectra of the samples, as seen in Figure 4.2, where the undoped-p(g3T2-T) shows a prominent absorption peak at 588 nm (red), which diminishes with doping, characteristic from oxidation, and it is more intense with higher doping levels. New absorption peaks are seen at around 860 nm, this is due to generation of polarons that lead to new optical transitions, as explained in section... from the Background chapter. Tan et al. described the apparition of new absorption peaks within 300

4. RESULTS AND DISCUSSION

to 600 nm, the higher energetic (lower wavelength) one is generated by unreacted neutral dopant species (TCNQ^0), while the second is due to the new dopant anions (TCNQ^-), the latter induce charges in our polymer [3]. It is shown also, that after some days of storage, the initially dominant peak of unreacted neutral dopants is now lower in intensity than the anions peak, suggesting that the dopants were still diffusing through the polymer along the days.

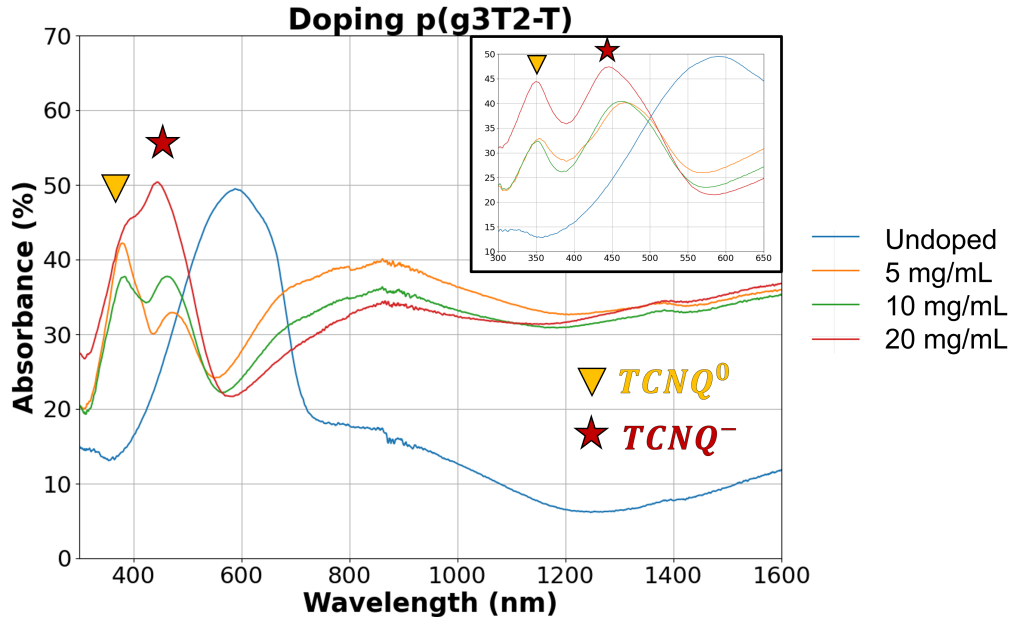


FIGURE 4.2: Spectra of undoped and doped-p(g3T2-T) at different doping levels, corresponding to samples on Figure 4.1. Inlet represents absorbance after two weeks of storage in ambient conditions.

Absorbance values are directly linked to the density of states of these new optical transitions [11]. From our spectra, the absorption value of the lowest doped-p(g3T2-T) (5 mg/mL) is higher (around 40%), which may be counter-intuitive. However, as doping concentration increases, hence more electrons are taken out of the polymer chain, a bipolaron is the energetically more favorable quasiparticle to generate. According to references [3][40], bipolaron formation is seen as a shift to lower energies in the broad absorbance the mid-IR region (wavenumber 1000-1600 cm^{-1}) so further analysis of hole bipolaron formation can be conducted with Fourier Transform InfraRed (FTIR) spectroscopy.

4.1.2 Workfunction

Although, the preparation of films for studying electron energy levels with UPS is ideally done under inert conditions to avoid any sort of contamination. The current fabrication process of OECTs inevitable exposes our films at ambient conditions. So

4.1. Doping Characterization

measurements were taken following the deposition under ambient conditions. Yet, it is possible to distinguish an increase in the workfunction (shift of Fermi level) of the polymer. The Fermi level shift towards the HOMO level is higher at higher dopant levels, as represented in Figure 4.3, characteristic of p-type doping. Some possible additional contamination did not allow to measure sample with 20 mg/mL of dopant, but tendency is evident.

TABLE 4.1: Workfunction calculation from UPS measurements.

	Undoped	5 mg/mL	10 mg/mL
E_{HBEC} [eV]	17.35	16.47	16.36
E_{HOMO} (vs E_F)	4.28	3.27	3.24
WF [eV]	3.87	4.28	4.86

It is important to consider that UPS is a surface sensitive measurement, the penetration depth of the ultraviolet range electrons are around 2 nm, which is significantly lower than our polymer thickness (around 70 nm). So this technique limits our understanding of the dopants diffusion through the whole volume of the polymer. Although, we had some insights of this topic from the previous section, further analysis could be done with X-Ray Photoelectron Spectroscopy that has a higher penetration depth (around 5 nm), again also limited.

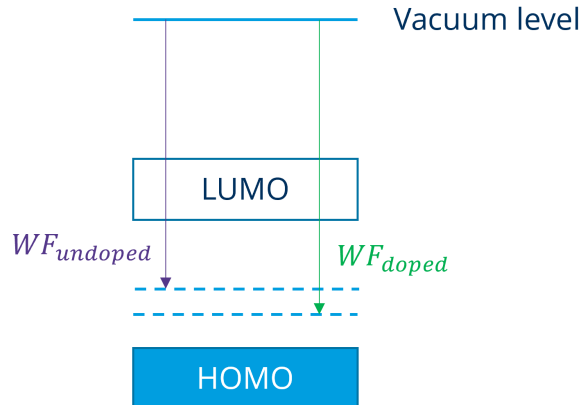


FIGURE 4.3: Representation of the Fermi level shift for doped-p(g3T2-t)

4.1.3 Thickness, Sheet Resistance and Resistivity

Sheet resistance and resistivity shown in Table 4.2 were calculated using equations 3.4 and 3.5, respectively, described in previous chapter. The film thickness was obtained with profilometer measurements, yielding to approximate 70 nm.

Upon doping there is a major decrease in both parameters, which is not as significant when adding more dopants, as seen in Figure 4.4. However, if comparing the decrease among doped samples, we could perceive a linear dependency upon increasing the dopant concentration.

4. RESULTS AND DISCUSSION

TABLE 4.2: Sheet resistance and resistivity calculations for undoped and doped films of p(g3T2-T)

	Undoped	5 mg/mL	10 mg/mL	20 mg/mL
Sheet resistance (Ω/sq)	6.3M	104.6k	70.7k	49.4k
Resistivity (Ωcm)	44.1	0.73	0.49	0.35

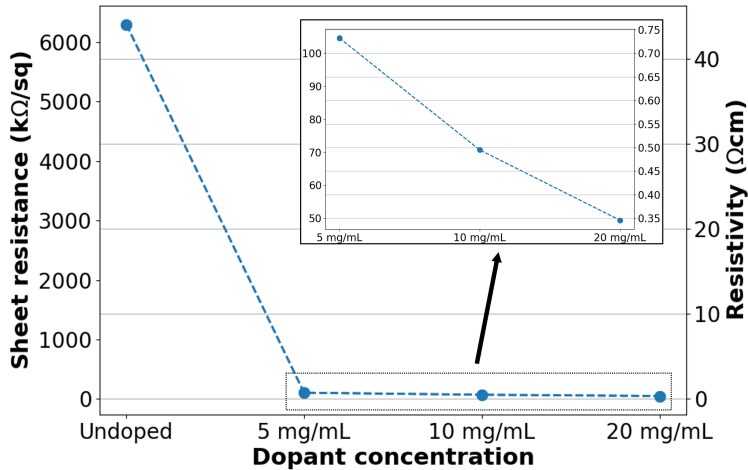


FIGURE 4.4: Sheet resistance and resistivity drop upon doping of p(g3T2-T). Inlet represents the quasi-linear drop of parameters as between doped samples.

4.2 Fabrication of Organic Electrochemical Transistors

4.2.1 Influence of Doping OECT Channel

The fabrication process used a mask that include a microstructure gate, available for studying OECTs with channel and gate made of the same OMIEC material (commonly PEDOT:PSS). The result of the patterning process is shown in Figure 4.5. However, in this part, we are going to test only the OMIEC channel (p(g3T2-T) at different doping levels) with a non-polarizable gate such as Ag/AgCl pellet, using dropcasted solid-state electrolyte precursor to couple both channel and gate. Unfortunately, the sample that used solution with 20 mg/mL dopant concentration showed homogeneity issues that still allow photolithography but could not represent a fair comparison with the other devices, so it will be disregarded in this analysis.

TABLE 4.3: Maximum transconductance and μC^* product calculation

	Undoped	5 mg/mL	10 mg/mL
$g_{m,max}$ [mS]	17.35	16.47	16.36
μC^* [$\text{Fcm}^{-1}\text{V}^{-1}\text{s}^{-1}$]	4.28	3.27	3.24

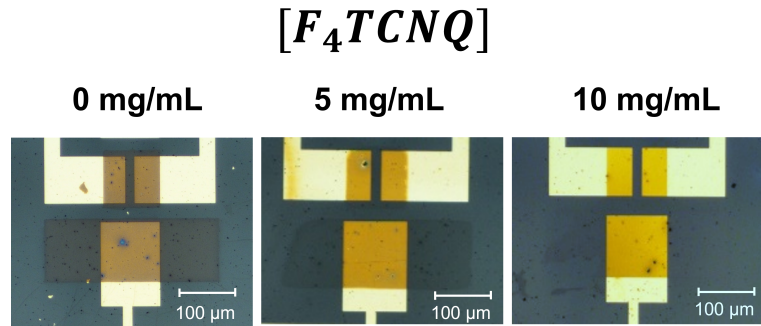


FIGURE 4.5: Micrographs of patterned channel and gate with undoped, 5 mg/mL and 10 mg/mL doped p(g3T2-T) following procedures explained in Section .

4.2.2 Stability on Air of p(g3T2-T)

4.2.3 Reverse Oxidation of Undoped-p(g3T2-T)

4.2.3.1 By Electrochemical Dedoping

4.2.3.2 By Heating

4.2.4 Solid-OEETs using Undoped p(g3T2-T)

4.2.4.1 Dropcasted Solid-State Electrolyte

4.2.4.2 OEET with Dropcast Solid-State Electrolyte

4.2.4.3 OEET with Photopatternable Solid-State Electrolyte

4.2.4.4 OEET with Inkjet-Printed Solid-State Electrolyte

4.2.5 Solid-OEETs using Doped-p(g3T2-T)

4. RESULTS AND DISCUSSION

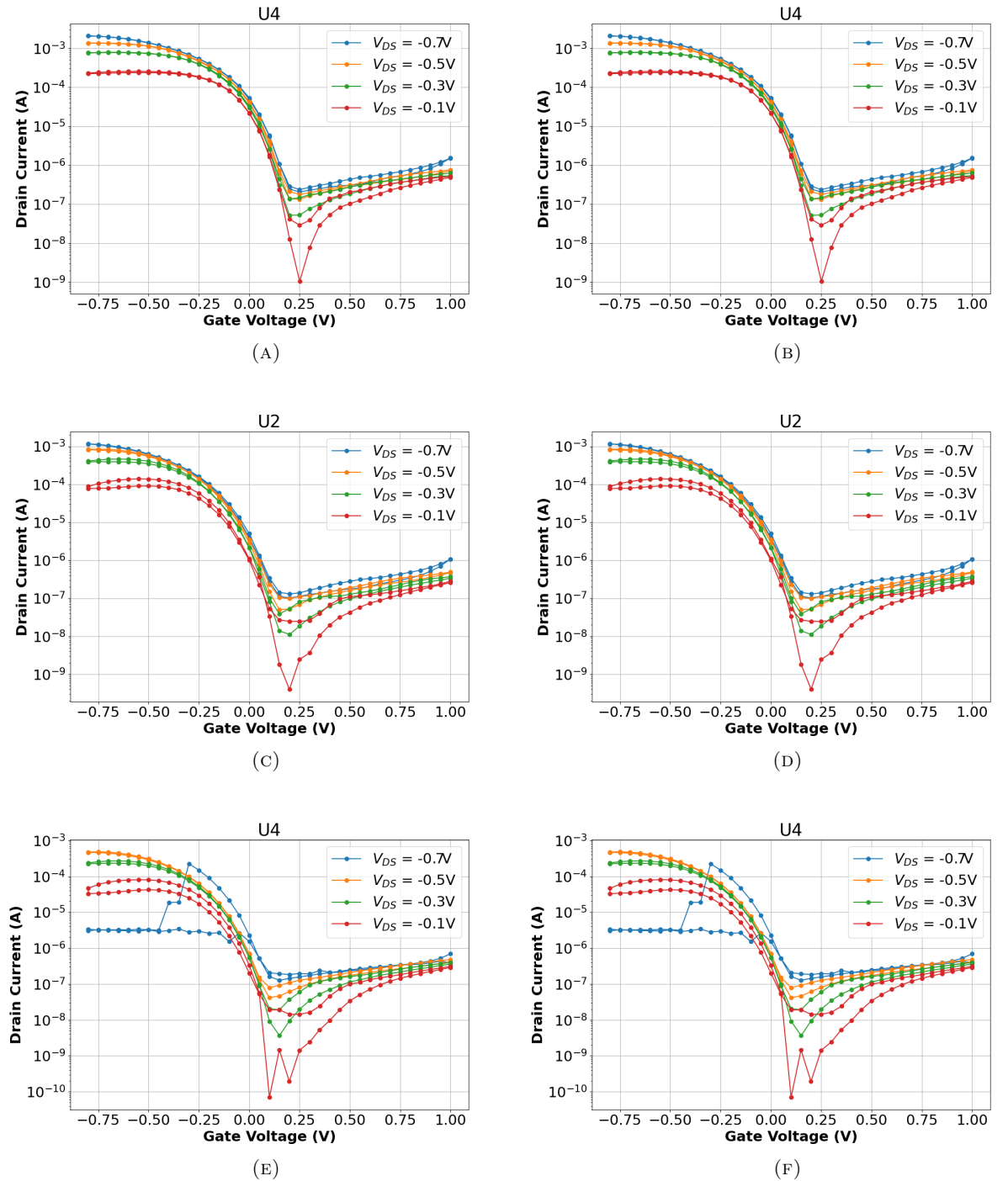


FIGURE 4.6: Transfer characteristics and transconductance at different V_{DS} . a), c) and e) correspond to the exponential behavior of undoped, 5 mg/mL and 10 mg/mL doped, respectively.

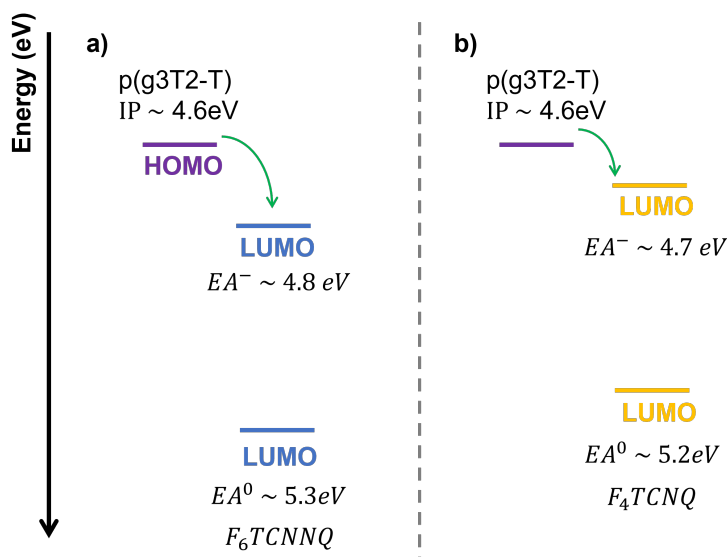


FIGURE 4.7: Energy diagram of p(g3T2-T) with a) F_6TCNNQ and b) F_4TCNNQ . Ionization potential of p(g3T2-T) extracted from reference [3] and electron affinities of the neutral species (EA^0) and of the anion (EA^-) of the dopants are extracted from cyclic voltammetry measurements in reference [12].

Chapter 5

Conclusions and Outlook

Besides the challenges of working with the conjugated polymer p(g3T2-T), due to its lower HOMO level that make it susceptible to molecular oxygen in ambient conditions and its highly volatile solvent, it was possible to successfully fabricate micro-structured accumulation-mode OECTs and solid-OECTs in ambient conditions. The section devoted to Doping characterization in the Results and Discussions Chapter demonstrated that it was possible to increase doping levels by using solution sequential doping. The level of homogeneity required to allow photopatterning processes was also achieved. However, accurate control of the doping level remains a challenge, an estimation of the molecular percentage of dopants cannot be assure due to the unknown quantity of dopants that succesfully diffuse throughout the thickness of the polymer, the characterization techniques used in this work present limitations to perform a full scanning of the doping level of the material within all its volume. Certainly, there is room for improvement in trying to achieve the level of control required.

Appendices

Appendix A

Absorption of p(g3T2-T) Doped with F6TCNNQ

Appendix B

PEDOT:PSS vs Doped p(g3T2-T) as Channel

Bibliography

- [1] J. Rivnay, S. Inal, A. Salleo, R. M. Owens, M. Berggren, and G. G. Malliaras, “Organic electrochemical transistors,” *Nature Reviews Materials*, vol. 3, no. 2, pp. 1–14, 2018.
- [2] C. B. Nielsen, A. Giovannitti, D.-T. Sbircea, E. Bandiello, M. R. Niazi, D. A. Hanifi, M. Sessolo, A. Amassian, G. G. Malliaras, J. Rivnay, and I. McCulloch, “Molecular Design of Semiconducting Polymers for High-Performance Organic Electrochemical Transistors,” *Journal of the American Chemical Society*, vol. 138, no. 32, pp. 10 252–10 259, 2016.
- [3] S. T. M. Tan, G. Lee, I. Denti, G. LeCroy, K. Rozylowicz, A. Marks, S. Griggs, I. McCulloch, A. Giovannitti, and A. Salleo, “Tuning Organic Electrochemical Transistor Threshold Voltage using Chemically Doped Polymer Gates,” *Advanced Materials*, vol. 34, no. 33, p. 2202359, 2022.
- [4] A. Weissbach, L. M. Bongartz, M. Cucchi, H. Tseng, K. Leo, and H. Kleemann, “Photopatternable solid electrolyte for integrable organic electrochemical transistors: Operation and hysteresis,” *Journal of Materials Chemistry C*, vol. 10, no. 7, pp. 2656–2662, 2022.
- [5] L. Alcácer, *Electronic Structure of Organic Semiconductors: Polymers and Small Molecules*. Morgan & Claypool Publishers, Dec. 2018.
- [6] A. J. Heeger, S. Kivelson, J. R. Schrieffer, and W. P. Su, “Solitons in conducting polymers,” *Reviews of Modern Physics*, vol. 60, no. 3, pp. 781–850, Jul. 1988.
- [7] M. Heydari Gharahcheshmeh and K. K. Gleason, “Texture and nanostructural engineering of conjugated conducting and semiconducting polymers,” *Materials Today Advances*, vol. 8, p. 100086, Dec. 2020.
- [8] J. L. Bredas, B. Themans, J. M. Andre, R. R. Chance, and R. Silbey, “The role of mobile organic radicals and ions (solitons, polarons and bipolarons) in the transport properties of doped conjugated polymers,” *Synthetic Metals*, vol. 9, no. 2, pp. 265–274, Apr. 1984.
- [9] B. Lüssem, M. Riede, and K. Leo, “Doping of organic semiconductors,” *physica status solidi (a)*, vol. 210, no. 1, pp. 9–43, 2013.

BIBLIOGRAPHY

- [10] M. L. Tietze, L. Burtone, M. Riede, B. Lüssem, and K. Leo, “Fermi level shift and doping efficiency in \$p\$-doped small molecule organic semiconductors: A photoelectron spectroscopy and theoretical study,” *Physical Review B*, vol. 86, no. 3, p. 035320, Jul. 2012.
- [11] J. L. Bredas and G. B. Street, “Polarons, bipolarons, and solitons in conducting polymers,” *Accounts of Chemical Research*, vol. 18, no. 10, pp. 309–315, Oct. 1985.
- [12] D. Kiefer, R. Kroon, A. I. Hofmann, H. Sun, X. Liu, A. Giovannitti, D. Stegerer, A. Cano, J. Hyynnen, L. Yu, Y. Zhang, D. Nai, T. F. Harrelson, M. Sommer, A. J. Moulé, M. Kemerink, S. R. Marder, I. McCulloch, M. Fahlman, S. Fabiano, and C. Müller, “Double doping of conjugated polymers with monomer molecular dopants,” *Nature Materials*, vol. 18, no. 2, pp. 149–155, Feb. 2019.
- [13] I. E. Jacobs, E. W. Aasen, J. L. Oliveira, T. N. Fonseca, J. D. Roehling, J. Li, G. Zhang, M. P. Augustine, M. Mascal, and A. J. Moulé, “Comparison of solution-mixed and sequentially processed P3HT:F4TCNQ films: Effect of doping-induced aggregation on film morphology,” *Journal of Materials Chemistry C*, vol. 4, no. 16, pp. 3454–3466, Apr. 2016.
- [14] S. T. M. Tan, “Organic Mixed Ionic Electronic Conductors for Electrochemical Devices,” Ph.D. dissertation, Stanford University, Palo Alto, CA, Dec. 2022.
- [15] A. Giovannitti, R. B. Rashid, Q. Thiburce, B. D. Paulsen, C. Cendra, K. Thorley, D. Moia, J. T. Mefford, D. Hanifi, D. Weiyuan, M. Moser, A. Salleo, J. Nelson, I. McCulloch, and J. Rivnay, “Energetic Control of Redox-Active Polymers toward Safe Organic Bioelectronic Materials,” *Advanced Materials*, vol. 32, no. 16, p. 1908047, 2020.
- [16] G. A. Snook, P. Kao, and A. S. Best, “Conducting-polymer-based supercapacitor devices and electrodes,” *Journal of Power Sources*, vol. 196, no. 1, pp. 1–12, Jan. 2011.
- [17] Y. Liang, Z. Tao, and J. Chen, “Organic Electrode Materials for Rechargeable Lithium Batteries,” *Advanced Energy Materials*, vol. 2, no. 7, pp. 742–769, 2012.
- [18] B. D. Paulsen, K. Tybrandt, E. Stavrinidou, and J. Rivnay, “Organic mixed ionic–electronic conductors,” *Nature Materials*, vol. 19, no. 1, pp. 13–26, Jan. 2020.
- [19] S. Wang, M. Ha, M. Manno, C. Daniel Frisbie, and C. Leighton, “Hopping transport and the Hall effect near the insulator–metal transition in electrochemically gated poly(3-hexylthiophene) transistors,” *Nature Communications*, vol. 3, no. 1, p. 1210, Nov. 2012.
- [20] S. T. M. Tan, A. Gumyusenge, T. J. Quill, G. S. LeCroy, G. E. Bonacchini, I. Denti, and A. Salleo, “Mixed Ionic–Electronic Conduction, a Multifunctional

BIBLIOGRAPHY

- Property in Organic Conductors,” *Advanced Materials*, vol. 34, no. 21, p. 2110406, 2022.
- [21] J. T. Friedlein, R. R. McLeod, and J. Rivnay, “Device physics of organic electrochemical transistors,” *Organic Electronics*, vol. 63, pp. 398–414, Dec. 2018.
 - [22] D. A. Bernards and G. G. Malliaras, “Steady-State and Transient Behavior of Organic Electrochemical Transistors,” *Advanced Functional Materials*, vol. 17, no. 17, pp. 3538–3544, 2007.
 - [23] S. Inal, G. G. Malliaras, and J. Rivnay, “Benchmarking organic mixed conductors for transistors,” *Nature Communications*, vol. 8, no. 1, p. 1767, Nov. 2017.
 - [24] S. T. Keene, T. P. A. van der Pol, D. Zakhidov, C. H. L. Weijtens, R. A. J. Janssen, A. Salleo, and Y. van de Burgt, “Enhancement-Mode PEDOT:PSS Organic Electrochemical Transistors Using Molecular De-Doping,” *Advanced Materials*, vol. 32, no. 19, p. 2000270, 2020.
 - [25] M. Moser, L. R. Savagian, A. Savva, M. Matta, J. F. Ponder, T. C. Hidalgo, D. Ohayon, R. Hallani, M. Reisjala, A. Troisi, A. Wadsworth, J. R. Reynolds, S. Inal, and I. McCulloch, “Ethylene Glycol-Based Side Chain Length Engineering in Polythiophenes and its Impact on Organic Electrochemical Transistor Performance,” *Chemistry of Materials*, vol. 32, no. 15, pp. 6618–6628, 2020.
 - [26] D. Moia, A. Giovannitti, A. A. Szumska, I. P. Maria, E. Rezasoltani, M. Sachs, M. Schnurr, P. R. F. Barnes, I. McCulloch, and J. Nelson, “Design and evaluation of conjugated polymers with polar side chains as electrode materials for electrochemical energy storage in aqueous electrolytes,” *Energy & Environmental Science*, vol. 12, no. 4, pp. 1349–1357, 2019.
 - [27] D. Ohayon, V. Druet, and S. Inal, “A guide for the characterization of organic electrochemical transistors and channel materials,” *Chemical Society reviews*, vol. 52, no. 3, pp. 1001–1023, 2023.
 - [28] T. Nguyen-Dang, K. Harrison, A. Lill, A. Dixon, E. Lewis, J. Vollbrecht, T. Hachisu, S. Biswas, Y. Visell, and T.-Q. Nguyen, “Biomaterial-Based Solid-Electrolyte Organic Electrochemical Transistors for Electronic and Neuromorphic Applications,” *Advanced Electronic Materials*, vol. 7, no. 12, p. 2100519, 2021.
 - [29] A. Savva, R. Hallani, C. Cendra, J. Surgailis, T. C. Hidalgo, S. Wustoni, R. Sheelamanthula, X. Chen, M. Kirkus, A. Giovannitti, A. Salleo, I. McCulloch, and S. Inal, “Balancing Ionic and Electronic Conduction for High-Performance Organic Electrochemical Transistors,” *Advanced Functional Materials*, vol. 30, no. 11, p. 1907657, 2020.
 - [30] A. Savva, C. Cendra, A. Giugni, B. Torre, J. Surgailis, D. Ohayon, A. Giovannitti, I. McCulloch, E. Di Fabrizio, A. Salleo, J. Rivnay, and S. Inal, “Influence of

BIBLIOGRAPHY

- Water on the Performance of Organic Electrochemical Transistors,” *Chemistry of Materials*, vol. 31, no. 3, pp. 927–937, Feb. 2019.
- [31] P. S. Foundation, “Miscellaneous operating system interfaces,” 2001-2023, date last access: 30-May-2023. [Online]. Available: <https://docs.python.org/3/library/os.html>
 - [32] ——, “Csv file reading and writing,” 2001-2023, date last access: 30-May-2023. [Online]. Available: <https://docs.python.org/3/library/csv.html>
 - [33] N. Developers, “Numpy user guide,” 2008 - 2022, date last access: 30-May-2023. [Online]. Available: <https://numpy.org/doc/stable/user/index.html#user>
 - [34] T. S. community, “Scipy.stats.linregress,” 2008-2023, date last access: 30-May-2023. [Online]. Available: <https://docs.scipy.org/doc/scipy/reference/generated/scipy.stats.linregress.html>
 - [35] G. avhn, “Peak detect library,” 2022, date last access: 30-May-2023. [Online]. Available: <https://github.com/avhn/peakdetect/blob/master/README.md>
 - [36] J. Hunter, D. Dale, E. Firing, M. Droettboom, and M. development team, “Matplotlib: Quick start guide,” 2012 - 2023, date last access: 30-May-2023. [Online]. Available: https://matplotlib.org/stable/tutorials/introductory/quick_start.html
 - [37] E. V. I. for Speciation Analysis (EVISA), “Instrument database: Shimadzu europe - solidsspec-3700/3700duv,” 2003-2010, date last access: 30-May-2023. [Online]. Available: <https://speciation.net/Database/Instruments/Shimadzu-Europe/SolidSpec37003700DUV-;i1305>
 - [38] S. A. Buchholtz, “Doping Properties of Novel Dopants for Organic Hole Transport Layers,” Ph.D. dissertation, Technische Universität Dresden, Dresden, Germany, nov 2021.
 - [39] L. M. Bongartz, “Organic electrochemical transistors with solid-state electrolytes,” Ph.D. dissertation, Technische Universität Dresden, Dresden, Germany, Jul. 2021.
 - [40] C. Enengl, S. Enengl, S. Pluczyk, M. Havlicek, M. Lapkowski, H. Neugebauer, and E. Ehrenfreund, “Doping-induced absorption bands in P3HT: Polarons and bipolarons,” *ChemPhysChem*, vol. 17, no. 23, pp. 3836–3844, 2016.